



# A multi-objective trajectory planning approach for vibration suppression of a series–parallel hybrid flexible welding manipulator

Caixia Ban<sup>a,c</sup>, Bing Fu<sup>d</sup>, Wei Wei<sup>a,d</sup>, Zhaotao Chen<sup>e</sup>, Shengnan Guo<sup>e</sup>,  
Nianchun Deng<sup>f</sup>, Lili Yuan<sup>b</sup>, Yu Long<sup>a,c,d,\*</sup>

<sup>a</sup> State Key Laboratory of Featured Metal Materials and Life-cycle Safety for Composite Structures, Guangxi University, Nanning, 530004, China

<sup>b</sup> Guangxi Key Laboratory of International Joint for China-ASEAN Comprehensive Transportation, Nanning University, Nanning, 530000, China

<sup>c</sup> School of Electrical Engineering, Guangxi University, Nanning 530004, China

<sup>d</sup> School of Mechanical Engineering, Guangxi University, Nanning 530004, China

<sup>e</sup> Guangxi Road and Bridge Engineering Group Co., Ltd, Nanning 530200, China

<sup>f</sup> School of Civil Engineering, Guangxi University, Nanning 530004, China

## ARTICLE INFO

Communicated by X. Jing

### Keywords:

Vibration suppression  
Hybrid welding manipulator  
Elastodynamics  
Trajectory planning

## ABSTRACT

Although the series–parallel hybrid welding manipulator has advantages over the traditional series manipulator, its must run continuously and smoothly according to a specific trajectory at the rated velocity. Considering a flexible manipulator with a complex series–parallel hybrid structure as the research object, this paper proposes a multi-objective approach to indirectly suppress the vibration. In view of the complex flexible mechanism with a multi-kinematic pair arrangement and a multi-motor drive, a system comprehensive elastodynamics model is established, and the effectiveness of the model is verified through the hammer test method. To achieve synchronous and coordinated planning of the end position and attitude, the spatial arc welding trajectory is planned on the basis of the synchronous planning controller and the dual-S velocity profile interpolation function. Then, a multi-objective optimization model considering the travel time, energy consumption and terminal amplitude fluctuations is proposed, the trajectory planning problem is transformed into a parameter optimization problem in the interpolation function, and then the elite non-dominated sorting genetic algorithm (NSGA-II) is employed to determine the optimal trajectory. The optimal trajectory thus obtained effectively suppresses the vibration of the system. Finally, compared with the classic fifth-degree polynomial trajectory planning method, the system vibration suppression effect is significant, which verifies the effectiveness and feasibility of the proposed method and provides a theoretical basis for further realizing real-time control.

## 1. Introduction

The series–parallel hybrid welding manipulator is an industrial robot that is used for arc welding tasks. It has the advantages of high motion precision, good flexibility, and flexible output. They belong to a class of highly coupled nonlinear systems with complex nonlinear dynamic behaviors. During welding operations, the manipulator must transition from its initial position to a specified location at a set velocity and along a predetermined path. However, due to the nonlinear characteristics of the structure resulting from the deformation of the elastic rod, the manipulator still has severe elastic vibration during and after the welding

\* Corresponding author.

E-mail addresses: [bancaixia@gxu.edu.cn](mailto:bancaixia@gxu.edu.cn) (C. Ban), [longyu@gxu.edu.cn](mailto:longyu@gxu.edu.cn) (Y. Long).

<https://doi.org/10.1016/j.ymssp.2024.111678>

Received 20 March 2024; Received in revised form 21 June 2024; Accepted 23 June 2024

Available online 3 July 2024

0888-3270/© 2024 Elsevier Ltd. All rights are reserved, including those for text and data mining, AI training, and similar technologies.

process. As a result, the operation is unstable, the end cannot reach the designated position quickly and accurately, the welding quality and work efficiency are reduced, and even fatigue damage occurs [1–4]. Therefore, to achieve fast, precise, and high-quality welding, it is necessary to investigate the vibration suppression of the welding manipulator.

Establishing a relatively accurate elastodynamics model of the welding manipulator is the premise for examining the vibration suppression of the system. Compared with the rigid body dynamics model, the elastodynamics model of the series–parallel hybrid welding manipulator is more complex, taking into account large-scale rigid motion and small-scale elastic deformation [5–7]. The main elastodynamic modeling methods are as follows: flexible multi-body system dynamics, kineto-elastodynamics(KED) method and dynamic substructure method [8]. Malgaca et al. [9,10] used finite element modeling of a composite box manipulator and analyzed the impact of the joint flexibility on the dynamic behavior of the system. Su et al. [11] conducted finite element modeling of a three-degree-of-freedom piezoelectric manipulator and analyzed the response displacement and resonance frequency under a given voltage signal. Mishra et al. [12] established a dynamic model of a two-link flexible manipulator with two revolute joints using the assumed mode method, and considered the time-varying natural frequency. Zhao et al. [13] considered the compliance of the limbs and joints of a five-degree-of-freedom hybrid machine tool and proposed a semi-analytical method to establish the elastodynamic equations. Xu et al. [14] adopted the finite element theory and KED method to establish an elastic dynamics model of the forging manipulator, and obtained its dynamic response using the Newmark stepwise integration method. Cai et al. [15,16] used the finite element method to establish an elastic dynamics model of an industrial robot based on beam elements in order to study the robot's dynamic response and chaos phenomena. Wu et al. [17] established the KED model of a delta robot based on the motion elastodynamics method, substructure synthesis technology, and Lagrange equation. Wang et al. [18] established a dynamic model of a flexible link plane-parallel platform using the substructure analysis method and obtained the basic dynamic behavior of the flexible link. Although several general manipulator dynamics models are available for some typical mechanical systems, there is a lack of accurate specific models for flexible robot mechanisms, considering the complex mechanisms involved in multi-kinematic pair arrangements and multi-motor drives.

Vibration suppression of flexible mechanical systems are mainly of two types. The first type is active control. Gao et al. [19] studied a full-state neural network controller and an output feedback neural network controller, and employed a two-link flexible manipulator as the test object to realize trajectory tracking and vibration suppression. Chou et al. [20] proposed a robust control methodology that uses an observer-based optimal model-following (OMF) controller to actively suppress the elastodynamic responses of the flexible linkage mechanism. Mohamed et al. [21] applied command shaping technology based on input shaping, low-pass and band-stop filtering to the feedforward control of flexible robots to suppress the vibration of the robot. Theodore et al. [22] proposed a robust controller based on Lyapunov's second method for the trajectory tracking of multi-link manipulators. The second type is indirect control. Wang et al. [23] proposed a multi-objective approach for the trajectory interpolated by quintic B-splines of a 7-DOF serial–parallel hybrid humanoid arm. Compared with the fifth-order polynomial methodology, the feasibility and effectiveness of the proposed methodology are validated through numerical simulations. Karagulle et al. [24,25] studied the effect of the trapezoidal velocity curve and the cycloid velocity profile on suppressing the residual vibration of the connecting rod. Chen et al. [26] proposed a multi-objective trajectory planning method based on an improved immune clonal selection algorithm for the 6-UPU parallel assembly platform (PAP). Results of trajectory simulation confirm that the demands of assembly task can be met. Abe [27] proposed a trajectory planning technology based on cubic splines to suppress the residual vibration of the dual-link rigid–flexible manipulator. The use of three different sets of initial and final joint angles shows that the residual vibrations are perfectly suppressed using the proposed method. Chen et al. [28] developed an optimal switching time control strategy combined with control parameters to suppress the residual vibration of a high-speed macro–micro manipulator system via trajectory planning. Spyrakos-Papastavridis et al. [29] introduced a minimum model-based trajectory tracking variable impedance control scheme to ensure the passivity/stability of a flexible joint robot. Therefore, for the problem of vibration suppression of manipulator in continuous arc welding operations, suppressing vibration through trajectory planning is an effective way, and there are no higher requirements for the controller. However, most of the above work only involves position trajectory planning, without considering attitude trajectory planning, which is equally important for robot posture adjustment. The trapezoidal velocity motion curve is the simplest and most commonly used trajectory planning method, but its acceleration will show discontinuity, causing the jerks to be infinite. By adopting the constrained step jerks and linear piece-wise acceleration, the S-curve profile can produce smoother transitions during the acceleration phase and deceleration phases [30]. Li et al. [31] proposed and optimized a general asymmetric S-curve profile to achieve fast motion and low residual vibration. Alzaydi et al. [32] presented a stitching algorithm for looping the same cluster trajectory and stitching between consecutive clusters based on modified s-curve profile, which guarantee a substantial improvement in the motion smoothness compared to using direct linear interpolation.

In this paper, we propose a method of indirectly suppressing the system vibration by optimizing trajectory parameters in order to achieve continuous tasks in a shorter time with lower energy consumption and higher stability. First, a comprehensive elastodynamics model of the complex system is established. Then, the dual-S speed profile interpolation function is used to plan the spatial arc welding trajectory to achieve collaborative consistency of the end position and attitude, and a synchronous planning controller is introduced to improve the motion control accuracy. In addition, the system vibration suppression objective function including travel time, energy consumption and amplitude fluctuations is established. Finally, the NSGA-II optimization program is used to achieve trajectory optimization.

The remainder of this paper is organized as follows. Section 2 gives an introduction about the hybrid welding manipulator and the trajectory planning method, and then establishes the kinematics model and rigid body dynamics model of the hybrid welding manipulator, respectively. Section 3 establishes the comprehensive elastodynamics model of the system and discusses its experimental verification. Section 4 describes the collaborative planning of the terminal pose using the dual-S velocity interpolation function method and proposes a multi-objective trajectory optimization method. Section 5 presents and discusses the results of numerical simulations. Finally, Section 6 concludes the paper and briefly explores directions for future work.

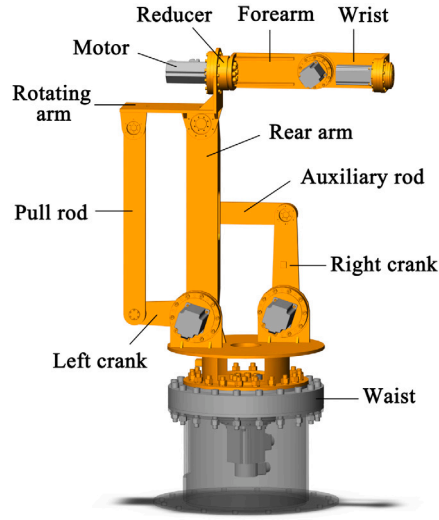


Fig. 1. 3D model of the hybrid welding manipulator.

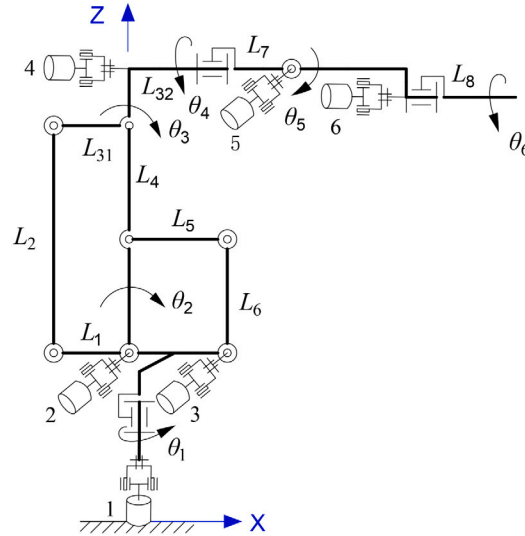


Fig. 2. Structure of the hybrid welding manipulator.

## 2. Hybrid welding manipulator and the trajectory planning method

Fig. 1 shows the 3D model of the hybrid welding manipulator. The robot under investigation is a multi-degree-of-freedom space series-parallel mechanism from a mechanical perspective. Its main components are the waist, left crank, pull rod, rotating arm, motor, reducer, forearm, wrist, rear arm, auxiliary rod, and right crank. The robotic mechanism consists of two partial parallelograms, the lengths of the tie rod and the rear arm are equal, and the length of the right crank is half of that of the rear arm. The servo motor drives the active rod (left crank) of the parallelogram mechanism on the left side to swing such that the rotating arm is supported by the pin shaft at the upper end of the rear arm to move up and down. In addition, the servo motor drives the active rod (right crank) of the right parallelogram mechanism to tilt the rear arm back and forth. As the pose of the end effector can be mainly determined from the joint angles of the waist, rear arm, rotating arm, forearm, and wrist, it is equivalent to an open-chain mechanism during kinematic analysis, and the kinematic relationship of the remaining rods can be driven indirectly. Each member is connected by a rotating pair, in which the pull rod, rear arm, and right crank remain parallel during movement.

Fig. 2 shows a schematic diagram of the structure of the hybrid welding manipulator, and the corresponding coordinate system is established in the figure. Each active joint is driven by a DC motor through a harmonic reducer. The global coordinate system is set at the bottom of the waist, and the numbers 1 to 6 denote the motor and reducer numbers. Through the motion of the six

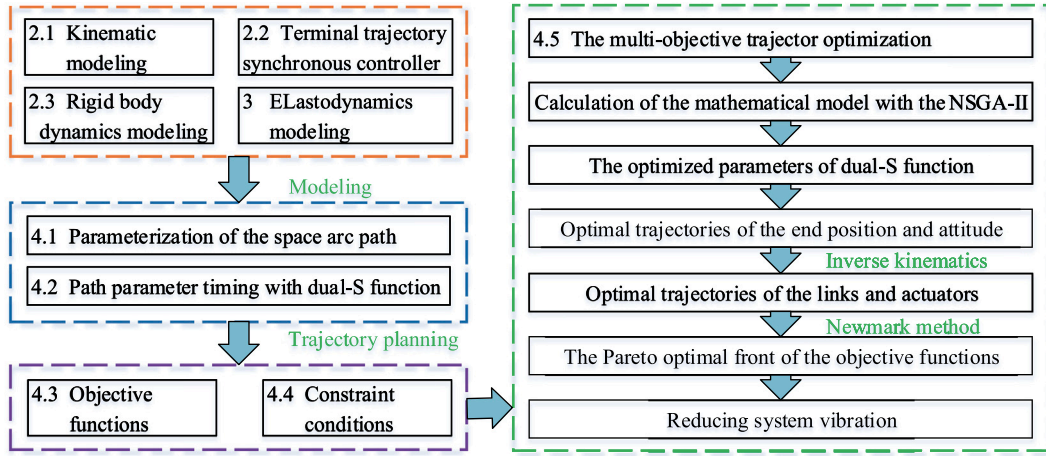


Fig. 3. The framework of the multi-objective vibration suppression method.

motors, the robot end effector can achieve movement along the three coordinate axes as well as rotation about the three coordinate axes.

To realize fast, smooth profile, and high-quality space arc welding operations, this paper proposes a multi-objective optimization method for the vibration suppression and the framework of this method is depicted in Fig. 3. The main idea is to first construct an arc welding trajectory with a consistent end position and attitude, and then optimize the parameters of the previously obtained trajectory according to the desired dynamic target.

### 2.1. Kinematics analysis

As the nominal trajectory of an end effector is usually planned in terms of its joint motion, the position and attitude of the end effector are functions of the joint angle  $\theta$ , i.e.,

$$\xi = \kappa(\theta) \quad (1)$$

where  $\xi \in \mathbb{R}^m$  denotes the position and posture of the end effector in the space coordinate system,  $m$  denotes the number of degrees of freedom of the end effector in the workspace,  $\theta \in \mathbb{R}^n$  denotes all the joint angles, and  $n$  denotes the number of joints.

Calculating the first and second derivatives relative to time from Eq. (1), we get

$$\begin{cases} \dot{\xi} = J\dot{\theta} \\ \ddot{\xi} = J\ddot{\theta} + \dot{J}\dot{\theta} \end{cases} \quad (2)$$

where  $\dot{\xi} \in \mathbb{R}^m$  denotes the space velocity of the end effector, including the translational and rotational velocity components;  $\ddot{\xi} \in \mathbb{R}^m$  denotes the spatial acceleration of the end effector, including the translational and rotational acceleration components; and  $J \in \mathbb{R}^{m \times n}$  denotes the Jacobian matrix of the manipulator, where  $J = d\kappa/d\theta$ ,  $\dot{J} = dJ/dt$ ,  $\dot{\theta} = d\theta/dt$ , and  $\ddot{\theta} = d\dot{\theta}/dt$ .

### 2.2. Design of terminal trajectory synchronous controller

The object of designing the terminal trajectory synchronous controller is to ensure that the terminal trajectory tracking error of the complex mechanical system stabilizes and approaches stability over time, thereby achieving synchronization between the actual and planned motions. The multiple variables for achieving synchronized motion include the maximum velocity (m/s), maximum acceleration ( $\text{m/s}^2$ ) and maximum jerk ( $\text{m/s}^3$ ) of the trajectory, which will be further explained in Section 5. By optimizing these variables, the system aims to achieve goals such as the shortest time, lowest energy consumption, and minimal amplitude, ultimately helping to indirectly dampen the elastic vibration of the system.

The synchronization error is defined as

$$\begin{cases} e_1 = \xi_s - \xi_m \\ e_2 = \dot{\xi}_s - \dot{\xi}_m \end{cases} \quad (3)$$

where  $e_1$  and  $e_2$  denote the position error and velocity error, respectively;  $\xi_m$  and  $\xi_s$  denote the end trajectories of the desired and actual manipulators, respectively.

Set the desired terminal trajectory equation as

$$\begin{cases} d\dot{\xi}_m/dt = \dot{\xi}_m \\ d\ddot{\xi}_m/dt = g(t) \end{cases} \quad (4)$$

where  $g(t)$  denotes the desired manipulator end trajectory acceleration equation.

By controlling the velocity and acceleration term of the terminal trajectory equation respectively, the actual terminal trajectory equation is

$$\begin{cases} d\dot{\xi}_s/dt = \dot{\xi}_s + u_1 \\ d\ddot{\xi}_s/dt = f(t) + u_2 \end{cases} \quad (5)$$

where  $f(t)$  denotes the actual manipulator end trajectory acceleration equation.;  $u_1$  and  $u_2$  denote the control terms added to the velocity and acceleration terms, respectively.

Design of second-order terminal trajectory synchronization controller

$$\begin{cases} u_1 = \dot{\xi}_m - \dot{\xi}_s + k_p e_1 \\ u_2 = g(t) - f(t) + k_v e_2 \end{cases} \quad (6)$$

where  $k_p$  and  $k_v$  denote negative definite gain matrices.

Assume a positive definite Lyapunov function

$$V(e_1, e_2) = (1/2)e_1^T e_1 + (1/2)e_2^T e_2 \quad (7)$$

When  $k_p$  and  $k_v$  are both negative definite diagonal matrices, the Lyapunov function is positive definite, and has

$$\dot{V} = e_1^T \dot{e}_1 + e_2^T \dot{e}_2 = k_p e_1^T e_1 + k_v e_2^T e_2 < 0 \quad (8)$$

Therefore, this control method is asymptotically stable. When  $t \rightarrow 0$ , the synchronization error asymptotically approaches 0.

The welding manipulator is a non-redundant mechanism, i.e.,  $J$  is a full-rank matrix. Therefore, if the end motion trajectory is known, the unique solution of the joint angular velocity and angular acceleration with the control term can be obtained as follows:

$$\begin{cases} \dot{\theta}_s = J^+(\dot{\xi}_m + k_p e_1) \\ \ddot{\theta}_s = J^+(\ddot{\xi}_m + k_v e_2 - \dot{J}\dot{\theta}_s) \end{cases} \quad (9)$$

where  $J^+ \in R^{n \times m}$  denotes the generalized inverse of  $J$ ;  $\dot{\theta}_s$  denotes the actual joint angular velocity, and  $\ddot{\theta}_s$  denotes the actual joint angular acceleration.

### 2.3. Rigid body dynamics analysis

The position of any point in the coordinate system of the  $i$ th link of the welding manipulator is denoted by  $r_i$ . Through multiplication with a transformation matrix  $T_i^0$  on the left-hand side, the position  $r_{ip}$  in the base coordinate system is obtained, i.e.,  $r_{ip} = T_i^0 r_i$ . The speed of this point is a function of the speed of all the joints; then, the velocity at this point is expressed as follows:

$$v_{ip} = \left( \sum_{j=1}^i U_{ij} \dot{q}_j \right) r_{ip} \quad (10)$$

$$U_{ij} = \begin{cases} T_{j-1}^0 Q_j^{j-1} T_i^j & (j \leq i) \\ 0 & (j > i) \end{cases} \quad (11)$$

The kinetic energy  $V_i$  of the robot links is the sum of the translational and rotational kinetic energies of each link. Furthermore, the total kinetic energy of the welding manipulator system includes the kinetic energy of each motor drive. Assuming that the inertia of each motor driver is  $I_{i(act)}$ , respectively, the kinetic energy of the corresponding driver is  $I_{i(act)} \dot{q}_i^2 / 2$ . Therefore, the total kinetic energy of the welding manipulator system is expressed as follows:

$$V = \frac{1}{2} \text{Trace} \left[ \sum_{i=1}^n \sum_{j=1}^i \sum_{k=1}^i U_{ij} J_i U_{ik}^T \dot{q}_j \dot{q}_k \right] + \frac{1}{2} \sum_{i=1}^n I_{i(act)} \dot{q}_i^2 \quad (12)$$

where  $J_i = \int r_i r_i^T dm_i$ .

The total potential energy of the welding manipulator system is denoted by  $P$ :

$$P = \sum_{i=1}^n [-m_i g^T \cdot (T_i^0 \bar{r}_{ip})] \quad (13)$$

where  $g^T = (0, 0, -|g|, 0)$ ,  $g$  denotes the gravity vector in the base coordinate,  $g = 9.8062 \text{ m/s}^2$ , and  $\bar{r}_{ip} = (\bar{x}_i, \bar{y}_i, \bar{z}_i, 1)^T$  denotes the position vector of the center of mass of the connecting rod in the base coordinate system.

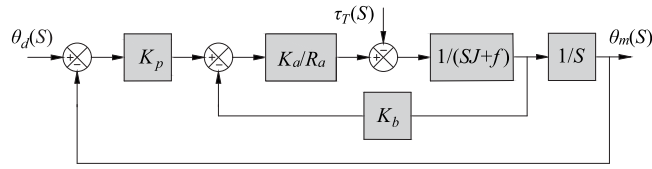


Fig. 4. Single-joint operation position feedback control.

The Lagrangian function of the welding manipulator system can be expressed as follows:

$$L = V - P \quad (14)$$

According to the Lagrange equation, the dynamic equation of the system is derived as follows:

$$\tau_i = \sum_{j=1}^n D_{ij} \ddot{q}_j + I_{i(act)} \ddot{q}_i + \sum_{j=1}^n \sum_{k=1}^n D_{ijk} \dot{q}_j \dot{q}_k + D_i \quad (15)$$

$$\begin{cases} D_{ij} = \sum_{p=\max(i,j)}^n \text{Trace}(U_{pj} J_p U_{pi}^T) \\ D_{ijk} = \sum_{p=\max(i,j,k)}^n \text{Trace}(U_{pjk} J_p U_{pi}^T) \\ D_i = \sum_{p=i}^n -m_p g^T U_{pi} \bar{r}_p \end{cases} \quad (16)$$

where the first term is the angular acceleration–inertia term, the second term is the drive inertia term, the third term is the Coriolis force and centrifugal force term, and the last term is the gravity term.

### 3. Elastodynamic modeling

The series–parallel hybrid flexible welding manipulator belongs to a type of highly coupled nonlinear system. The flexibility of connecting rods, joints and drive components causes the manipulator to vibrate during welding operations, reducing the accuracy of position and force control, and potentially causing structural resonance. It is necessary to establish a relatively accurate elastic dynamics model to study the vibration characteristics of the system.

According to the structure and motion characteristics of the welding manipulator, we propose to combine the KED method and substructure synthesis technology to reduce the system model and establish a comprehensive elastodynamics model of the complex welding manipulator. The system can be decomposed into several substructures with different properties, such as the drive system substructure, transmission system substructure, elastic rod substructure, and bearing substructure. The dynamic equations of the various substructures are deduced separately, and then, by introducing deformation compatibility conditions, the comprehensive elastodynamics model of the whole system will be established.

Owing to the high stiffness of the industrial manipulator, its elastic deformation is extremely small. To simplify the calculation with higher accuracy, the following assumptions are made:

- (1) Ignoring the coupling of rigid body motion and elastic deformation, the real motion can be regarded as a linear superposition of the two motions.
- (2) Assuming an instantaneous structure, at a certain mechanism position, the rotating coordinate system, rotation angle, and rotation matrix do not change.
- (3) The inertia of the flexible wheel and the connecting piece can be ignored, and the inertia of the wave generator is converted to the motor rotor.
- (4) Ignore the effects of clearance and friction.

#### 3.1. Differential equations of the drive system substructure

Each active joint of the hybrid welding manipulator is driven by a servo motor. The relationship between the motor voltage  $U_d(S)$  and the angular displacement  $\theta_m(S)$  is expressed as follows:

$$\theta_m(S) = \frac{K_a U_d(S) - \tau_T(S)(S L_a + R_a)}{S(S^2 J L_a + S(L_a f + R_a) + R_a f + K_a K_b)} \quad (17)$$

where  $\theta_m(S)$  denotes the Laplace transform of the motor rotation angle,  $U_d(S)$  denotes the pull-type transformation of a given voltage,  $L_a$  denotes the armature inductance,  $R_a$  denotes the armature resistance,  $\tau_T(S)$  denotes the motor output torque pull conversion,  $K_a$  denotes the motor torque proportional constant,  $K_b$  denotes the speed coefficient,  $J$  denotes the inertia moment of a single motor rotor, and  $f$  denotes the viscous friction coefficient.

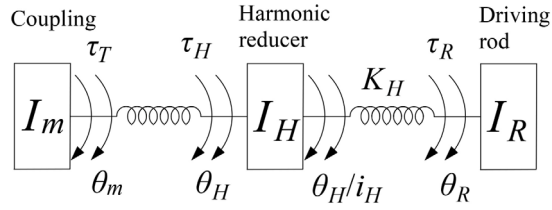


Fig. 5. The diagram of the transmission system.

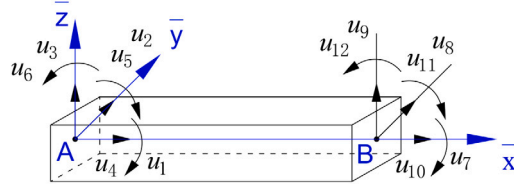


Fig. 6. Model of spatial beam elements.

Considering that  $L_a$  is small, we can omit it. The block diagram of the position feedback control system based on the proportional adjustment controller is shown in Fig. 4, and the following relationship can be obtained:

$$((\theta_d(S)K_p - \theta_m(S)K_p - K_b S \theta_m(S)) \frac{K_a}{R_a} - \tau_T(S)) \frac{1}{S I_m + f} = S \theta_m(S) \quad (18)$$

where  $K_p$  is the gain coefficient of the proportional regulator.

The second-order motion differential equation of each active joint drive system is expressed in the time domain as follows:

$$I_m \ddot{\theta}_m + C_m \dot{\theta}_m + K_m \theta_m = K_m \theta_d - \tau_T \quad (19)$$

$$\begin{cases} C_m = \frac{K_a K_b}{R_a} + f \\ K_m = \frac{K_a K_p}{R_a} \end{cases} \quad (20)$$

where  $I_m$  denotes the motor rotor's moment of inertia;  $C_m$  denotes the motor rotor's damping,  $C_m = K_a K_b / R_a + f$ ;  $K_m$  denotes the motor rotor's stiffness,  $K_m = K_a K_p / R_a$ ;  $\theta_m$ ,  $\dot{\theta}_m$ , and  $\ddot{\theta}_m$  denote the output angle, output angular velocity, and output angular acceleration of the motor, respectively;  $\tau_T$  denotes the motor's output torque, i.e., the input torque of the transmission system; and  $\theta_d$  denotes a fixed value of zero for a certain instantaneous fixed structure.

As can be seen from Eq. (19), when the rotation angle  $\theta_d$  is given, the motor generates a torque  $K_m \theta_d$  under the action of the control system, part of which is used to drive the transmission mechanism and the various rods connected to it, while the other part is used to drive the rotor of the motor itself.

### 3.2. Differential equations of the transmission substructure

The transmission system of the hybrid welding manipulator comprises couplings, harmonic reducers, transmission shafts, and other transmission parts. The harmonic reducer consists of three basic components, namely, the wave generator, flexible wheel, and steel wheel. Ignoring the influence of the coupling, it is considered that the motor output torque acts directly on the harmonic reducer, i.e.,  $\tau_T = \tau_H$ ,  $\theta_m = \theta_H$ . The transmission system is a multi-degree-of-freedom torsional vibration system. The calculation diagram is shown in Fig. 5.

Take the moment balance equation for  $I_H$  as follows:

$$\begin{cases} \tau_H = I_H \ddot{\theta}_H + K_H (\frac{\theta_H}{i_H^2} - \frac{\theta_R}{i_H}) + C_H (\frac{\dot{\theta}_H}{i_H^2} - \frac{\dot{\theta}_R}{i_H}) \\ \tau_R = i_H \tau_H \end{cases} \quad (21)$$

Rewriting Eq. (21) in matrix form, we can obtain the dynamic equation of the transmission system:

$$\mathbf{M}_t \ddot{\theta}_t + \mathbf{C}_t \dot{\theta}_t + \mathbf{K}_t \theta_t = \mathbf{Q}_t \quad (22)$$

$$\begin{cases} \mathbf{M}_t = \text{diag} [I_H & 0] \\ \mathbf{C}_t = \begin{bmatrix} C_H/i_H^2 & -C_H/i_H \\ -C_H/i_H & C_H \end{bmatrix} \\ \mathbf{K}_t = \begin{bmatrix} K_H/i_H^2 & -K_H/i_H \\ -K_H/i_H & K_H \end{bmatrix} \\ \mathbf{Q}_t = [\tau_H & -\tau_R] \\ \boldsymbol{\theta}_t = [\theta_H & \theta_R] \end{cases} \quad (23)$$

where  $\mathbf{M}_t$ ,  $\mathbf{C}_t$ ,  $\mathbf{K}_t$  and  $\mathbf{Q}_t$  denote the mass matrix, damping matrix, stiffness matrix, and force matrix of the transmission system, respectively;  $I_H$  denotes the moment of inertia of the harmonic reducer, which is typically ignored;  $C_H$  denotes the transmission damping coefficient;  $K_H$  denotes the stiffness coefficient of the flexible wheel;  $i_H$  denotes the speed ratio of the harmonic reducer;  $\tau_T$  denotes the output of the motor;  $\tau_R$  denotes the input torque of the driving rod; and  $\theta_t$  denotes the angular displacement,  $\dot{\theta}_t$  and  $\ddot{\theta}_t$  are the first and second derivatives of  $\theta_t$ , respectively.

### 3.3. Differential equations of flexible arm substructures

#### 3.3.1. Spatial beam element model

Fig. 6 shows an equal-section space beam element. First, the element coordinate system  $A-\bar{x}\bar{y}\bar{z}$  of the beam element is established, where the two nodes of the beam element are  $A$  and  $B$ . The  $\bar{x}$  axis of the element coordinate system coincides with the longitudinal axis of the element, while the  $\bar{y}$  and  $\bar{z}$  axes follow the right-hand helix rule. The spatial beam element is elastically deformed along the three coordinate axes, and the vector  $\mathbf{u} = [u_1, u_2, \dots, u_{12}]^T$  of the element coordinates is established. Further,  $u_1 - u_3$  and  $u_7 - u_9$  denote the linear displacements and  $u_4 - u_6$  and  $u_{10} - u_{12}$  denote the angular displacements of nodes  $A$  and  $B$ , respectively. According to the working accuracy requirements and boundary conditions of the industrial robot, the following equation can be obtained:

$$\begin{bmatrix} W_x(x, t) \\ W_y(x, t) \\ W_z(x, t) \\ \varphi_x(x, t) \\ \varphi_y(x, t) \\ \varphi_z(x, t) \end{bmatrix} = \begin{bmatrix} \mathbf{N}_A^T \\ \mathbf{N}_B^T \\ \mathbf{N}_C^T \\ \mathbf{N}_D^T \\ \dot{\mathbf{N}}_C^T \\ \dot{\mathbf{N}}_B^T \end{bmatrix} \mathbf{u} = \mathbf{N} \mathbf{u} \quad (24)$$

$$\begin{cases} \mathbf{N}_A = [n_1, 0, 0, 0, 0, 0, n_2, 0, 0, 0, 0, 0]^T \\ \mathbf{N}_B = [0, n_3, 0, 0, 0, 0, n_4, 0, n_5, 0, 0, 0]^T \\ \mathbf{N}_C = [0, 0, n_3, 0, -n_4, 0, 0, 0, n_5, 0, -n_6, 0]^T \\ \mathbf{N}_D = [0, 0, 0, n_1, 0, 0, 0, 0, 0, n_2, 0, 0]^T \\ n_1 = 1 - e & n_2 = e \\ n_3 = 2e^3 - 3e^2 + 1 & n_4 = L(2e^2 - e - e^3) \\ n_5 = 3e^2 - 2e^3 & n_6 = L(2e^2 - e^3) \end{cases} \quad (25)$$

where  $W_x(x, t)$ ,  $W_y(x, t)$ , and  $W_z(x, t)$  denote the linear displacement functions along the  $x$ ,  $y$ , and  $z$  directions, respectively;  $\varphi_x$ ,  $\varphi_y$ , and  $\varphi_z$  denote the angular displacement functions along the  $x$ ,  $y$ , and  $z$  directions, respectively;  $L$  is the unit length;  $e$  is the relative coordinate,  $e = x/L$ ; and  $n_i$  ( $i = 1, 2, \dots, 6$ ) is the displacement shape function.

#### 3.3.2. Beam element kinetic energy

Assuming that the section of the spatial beam element is a uniform rectangular section and the mass at the section is concentrated on the axis, and ignoring the rotational kinetic energy of the section in the  $y$  and  $z$  directions, we can express the kinetic energy  $E_k$  of the beam element as follows:

$$\begin{aligned} E_k &= \frac{1}{2} \rho [A(\dot{W}_x^2 + \dot{W}_y^2 + \dot{W}_z^2) + I_p \dot{\theta}^2] dx \\ &= \frac{1}{2} \dot{\mathbf{u}}_a^T \bar{\mathbf{m}} \dot{\mathbf{u}}_a \end{aligned} \quad (26)$$

where  $\rho$  denotes the density,  $A$  denotes the cross-sectional area,  $I_p$  denotes the polar moment of inertia of the element cross section about the  $x$  axis, and  $\bar{\mathbf{m}}$  denotes the element mass matrix.

$$\dot{\mathbf{u}}_a = \dot{\mathbf{u}} + \dot{\mathbf{u}}_r \quad (27)$$

where  $\dot{\mathbf{u}}_a$  denotes the absolute motion speed,  $\dot{\mathbf{u}}$  denotes the elastic motion speed, and  $\dot{\mathbf{u}}_r$  denotes the rigid body motion speed.



### 3.3.3. Beam element potential energy

The potential energy of the element includes the tensile and compressive deformation energies caused by the force in the direction of each coordinate axis of the beam element, as well as the bending deformation energy caused by the bending moment and the torsional deformation energy caused by the torque. The potential energy  $E_p$  of the beam element can be expressed as follows:

$$\begin{aligned} E_p &= \frac{1}{2} E \int_0^L [A(W'_x)^2 + I_z(W''_y)^2 + I_y(W''_z)^2] dx + \frac{1}{2} G I_p \int_0^L (\theta'_x)^2 dx \\ &= \frac{1}{2} \mathbf{u}^T \bar{\mathbf{k}} \mathbf{u} \end{aligned} \quad (28)$$

where  $E$  denotes the elastic modulus of the beam element,  $G$  denotes the shear elastic modulus of the beam element,  $I_y$  denotes the moment of inertia of the section in the  $xz$  coordinate plane,  $I_z$  denotes the moment of inertia of the section in the  $xy$  coordinate plane, and  $\bar{\mathbf{k}}$  denotes the element stiffness matrix.

### 3.3.4. Beam element dynamic equations

By substituting Eq. (26) and Eq. (28) into the Lagrangian equation of the second type, we can obtain the dynamic equation of the space beam element as follows:

$$\bar{\mathbf{m}}\ddot{\mathbf{u}} + \bar{\mathbf{k}}\mathbf{u} = \bar{\mathbf{f}} - \bar{\mathbf{m}}\ddot{\mathbf{u}}_r \quad (29)$$

where  $\bar{\mathbf{f}}$  denotes the generalized force array of the unit, including the driving external moment  $\tau_R$  and the force acting on the unit by the adjacent unit through the node;  $\mathbf{u}$  denotes the elastic displacement matrix;  $\ddot{\mathbf{u}}$  denotes the elastic acceleration matrix; and  $\ddot{\mathbf{u}}_r$  denotes the rigid body acceleration matrix.

To facilitate the assembly of the differential equation of motion of the beam element into the equation of motion of the substructure system, we introduce a new element generalized coordinate array:

$$\mathbf{u}_e = [u_{e1}, u_{e2}, \dots, u_{e12}]^T \quad (30)$$

According to assumption (2),  $\mathbf{u}$  and  $\mathbf{u}_e$  have the following relationship:

$$\mathbf{u} = \mathbf{R}\mathbf{u}_e \quad (31)$$

where  $\mathbf{R}$  denotes the coordinate transformation matrix.

The differential equation of motion of the beam element in the absolute coordinate system is expressed as follows:

$$\mathbf{m}\ddot{\mathbf{u}}_e + \mathbf{k}\mathbf{u}_e = \mathbf{f} - \mathbf{m}\ddot{\mathbf{u}}_{er} \quad (32)$$

where  $\mathbf{m} = \mathbf{R}^T \bar{\mathbf{m}} \mathbf{R}$ ,  $\mathbf{k} = \mathbf{R}^T \bar{\mathbf{k}} \mathbf{R}$ , and  $\mathbf{f} = \mathbf{R}^T \bar{\mathbf{f}}$ .  $\mathbf{m}$  denotes the element equivalence mass matrix,  $\mathbf{k}$  denotes the element equivalence stiffness matrix,  $\mathbf{f}$  denotes the element equivalence force matrix,

### 3.3.5. Dynamic equation of flexible rod structure

The flexible pole structure consists of several space beam units, and the dynamic equations of all the unit elements of the flexible pole are composed of the dynamic equations of the flexible pole structure according to the displacement coordination matrix. According to the structural characteristics of the hybrid welding robot, the left crank, right crank, and wrist are cantilever beams, the tie rod and the rear arm are divided into two units, and the remaining rods are one unit. The flexible pole structure of the hybrid welding robot has a total of 11 units. Define the system generalized coordinate array as follows:

$$\mathbf{u}_R = [u_{R1}, u_{R2}, \dots, u_{RN_u}]^T \quad (33)$$

where  $N_u$  denotes the total number of generalized coordinates, i.e.,  $N_u = 57$ .

The relationship between  $\mathbf{u}_e$  and  $\mathbf{u}_R$  is expressed as follows:

$$\mathbf{u}_e = \mathbf{b}_i \mathbf{u}_R \quad (34)$$

where  $\mathbf{b}_i$  is the coordinate coordination matrix of the flexible pole structure.

The unit motion differential equation with the system coordinates of the overall number as the unknown is expressed as follows:

$$\mathbf{M}_i^e \ddot{\mathbf{u}}_R + \mathbf{K}_i^e \mathbf{u}_R = \mathbf{F}_i^e - \mathbf{M}_i^e \ddot{\mathbf{u}}_{Rr} \quad (35)$$

where  $\mathbf{M}_i^e = \mathbf{b}_i^T \mathbf{m}_i \mathbf{b}_i$ ,  $\mathbf{K}_i^e = \mathbf{b}_i^T \mathbf{k}_i \mathbf{b}_i$ , and  $\mathbf{F}_i^e = \mathbf{b}_i^T \mathbf{f}_i$ .

In the process of studying the actual work of the flexible pole structure of the hybrid welding robot, the influence of damping cannot be ignored. The Rayleigh damping matrix is used to include the elastic dynamic equation of the flexible pole structure. The sum of all the unit dynamic equations gives the differential equation of motion for the flexible rod structure:

$$\mathbf{M}_R \ddot{\mathbf{u}}_R + \mathbf{C}_R \dot{\mathbf{u}}_R + \mathbf{K}_R \mathbf{u}_R = \mathbf{F}_R - \mathbf{M}_R \ddot{\mathbf{u}}_{Rr} \quad (36)$$

where the subscript  $R$  represents the flexible pole structure;  $\ddot{\mathbf{u}}_{Rr}$  denotes the rigid body acceleration array of the flexible pole structure system;  $\mathbf{M}_R = \sum_{i=1}^{N_e} \mathbf{M}_i^e$ ,  $\mathbf{C}_R = \sum_{i=1}^{N_e} \mathbf{C}_i^e$ ,  $\mathbf{K}_R = \sum_{i=1}^{N_e} \mathbf{K}_i^e$ , and  $\mathbf{F}_R = \sum_{i=1}^{N_e} \mathbf{F}_i^e$  are the mass matrix, damping matrix, stiffness matrix, and generalized force array of the flexible pole structure, respectively; and  $N_e$  is the total number of elements of the flexible pole structure, i.e.,  $N_e = 11$ .

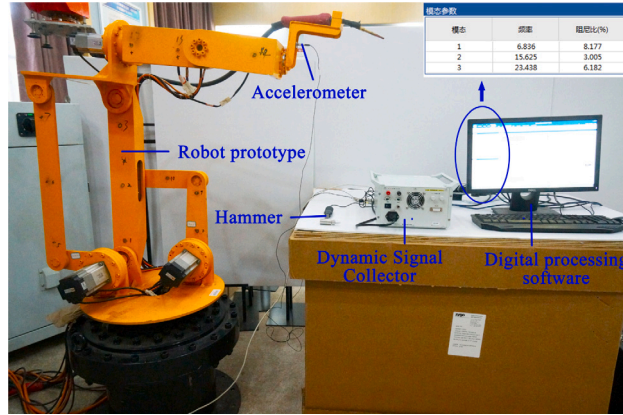


Fig. 7. The hammering tests of the welding manipulator.

### 3.4. Bearing substructure

The rotating joints of articulated robots employ crossed-roller bearings, which can better withstand radial and axial forces compared to common ball bearings and thrust bearings. Hence, they are ideal for articulated robots.

As the overall mass of the bearing is much smaller than the mass of the motor, reducer, and robot rod, the system does not consider the mass of the bearing. The modeling of the bearings mainly considers the stiffness model that significantly affects the dynamic behavior of the system. According to the Hertz contact theory, the bearing stiffness matrix is obtained by calculating the relationship between the bearing load and the contact deformation, which includes the radial stiffness, axial stiffness, and angular stiffness. The bearing is simplified as a linear matrix representing the support characteristics and added to the dynamic equation established using the finite element method.

The relative displacement vector of the bearing unit nodes with three translational and three rotational degrees of freedom is expressed as follows:

$$\mathbf{u}_b = [u_x, u_y, u_z, \theta_x, \theta_y, \theta_z]^T \quad (37)$$

where  $u_x$ ,  $u_y$ , and  $u_z$  represent the displacement in the direction of the  $x$ ,  $y$ , and  $z$  axis, respectively, and  $\theta_x$ ,  $\theta_y$ , and  $\theta_z$  represent the rotation angle about the direction of the  $x$ ,  $y$ , and  $z$  axis respectively.

In general, the linearized bearing can be simulated by six stiffness coefficients and six damping coefficients. The dynamic equation of the bearing is expressed as follows:

$$\mathbf{C}_b \dot{\mathbf{u}}_b + \mathbf{K}_b \mathbf{u}_b = \mathbf{f}_b \quad (38)$$

where  $\mathbf{C}_b = \text{diag}(c_x, c_y, c_z, c_{\theta_x}, c_{\theta_y}, c_{\theta_z})$  and  $\mathbf{K}_b = \text{diag}(k_x, k_y, k_z, k_{\theta_x}, k_{\theta_y}, k_{\theta_z})$ . The values for the remaining degrees of freedom of the bearing matrix are zero. Further,  $\mathbf{f}_b$  denotes the external force vector received by the bearing.

### 3.5. Differential equations of the hybrid welding robot system

According to the position of the drive system substructure, transmission system substructure, flexible rod structure, and bearing substructure in the system, the continuity condition and displacement coordination matrix of each substructure are used to assemble and calculate the overall matrix equation of the hybrid welding robot system. The hybrid welding robot system is divided into 6 drive system substructures, 6 transmission system substructures, and 11 flexible rod unit substructures. The system has a total of 63 degrees of freedom.

The relationship between the generalized coordinates of the individual substructures and the system generalized coordinates is expressed as follows:

$$\mathbf{u}_i = \mathbf{B}_i \mathbf{U} \quad (39)$$

where  $\mathbf{u}_i$  denotes the generalized coordinate of the  $i$ th substructure;  $\mathbf{U}$  denotes the generalized coordinate of the entire hybrid welding robot system; and  $\mathbf{B}_i$  denotes the system coordination matrix, which is a matrix of  $12 \times N_u$ , and its elements are all 0 or 1.

By substituting  $\mathbf{u}_i$  into each substructure equation, pre-multiplying  $\mathbf{B}_i^T$ , and finally adding up each equation, the elastic dynamic equation of the hybrid welding robot system can be calculated as follows :

$$\mathbf{M} \ddot{\mathbf{U}} + \mathbf{C} \dot{\mathbf{U}} + \mathbf{K} \mathbf{U} = \mathbf{F} - \mathbf{M} \ddot{\mathbf{U}}_r \quad (40)$$

**Table 1**  
Material characteristic parameters and moment of inertia of the welding manipulator.

Component	Left crank	Pull rod	Rotating arm		Rear arm	Auxiliary rod	Right crank	Forearm	Wrist
Length (m)	$L_1$	$L_2$	$L_{31}$	$L_{32}$	$L_4$	$L_5$	$L_6$	$L_7$	$L_8$
	0.2	0.6	0.2	0.1725	0.6	0.26	0.3	0.366	0.257
	$L_{s1}$	$L_{s2}$	–	–	$L_{s4}$	$L_{s5}$	$L_{s6}$	–	–
	0.1	0.3	–	–	0.3	0.13	0.15	–	–
Mass (kg)	1.677	4.222	4.274	2	12.68	1.994	2.440	3.699	3.145
Moment of inertia (kg m <sup>2</sup> )	$8.40 \times 10^{-3}$	$1.474 \times 10^{-1}$	$3.026 \times 10^{-2}$	$3.026 \times 10^{-2}$	$4.443 \times 10^{-1}$	$1.681 \times 10^{-2}$	$2.314 \times 10^{-2}$	$7.633 \times 10^{-3}$	$2.816 \times 10^{-2}$

**Table 2**  
Parameters of six motors and reducers in the system.

Number	$I_m$	$C_m$	$K_m$	$C_H$	$K_H$	$i_H$
1	$3.9e^{-3}$	0.142	130	76.2	$1.27e^5$	100
2,3,4	$2.5e^{-3}$	0.21	50	76.2	$1.8e^5$	50
5,6	$1.5e^{-3}$	0.34	80	76.2	$1.6e^5$	80

Units: kg m<sup>2</sup>, N m s/rad, N m/rad.

**Table 3**  
Bearing parameters.

Stiffness	$k_x$	$k_y$	$k_z$	$k_{\theta x}$	$k_{\theta y}$	$k_{\theta z}$
Value (N/m)	$2.1e^{-3}$	0.142	89	76.2	$1.27e^5$	100
Damping	$c_x$	$c_y$	$c_z$	$c_{\theta x}$	$c_{\theta y}$	$c_{\theta z}$
Value (Ns/m)	500	500	500	700	700	700

**Table 4**  
Comparison of natural frequency experimental test and numerical analysis.

	$f_1$	$f_2$	$f_3$
Experimental test results (Hz)	6.836	15.625	23.438
Numerical Analysis Results (Hz)	6.892	16.157	24.293
error	0.8%	3.4%	3.65%

where  $\mathbf{M}$ ,  $\mathbf{C}$ , and  $\mathbf{K}$  denote the overall mass matrix, overall damping matrix, and overall stiffness matrix vector of the system, respectively;  $\mathbf{F}$  denotes overall load vector; and  $\mathbf{U}$ ,  $\dot{\mathbf{U}}$ , and  $\ddot{\mathbf{U}}$  denote the overall nodal displacement, nodal velocity, and nodal acceleration vectors, respectively.

From the dynamic equation of the welding manipulator system, we can see that the stiffnesses of the drive system, transmission system, elastic member, and bearing in the overall stiffness matrix are the intrinsic factors underlying the nonlinear vibration of the system. The external excitation is expressed in the load column vector, which coupling with the intrinsic factors in the system enhances the nonlinear dynamic characteristics of the welding manipulator system. Therefore, we must conduct vibration reduction analysis for the welding manipulator system.

### 3.6. Elastodynamic model validation

To verify the accuracy of the proposed elastic dynamic model, we conducted experimental modal analysis of the mechanical arm prototype using the most classical single-point pickup vibration test method, as shown in Fig. 7. To obtain a higher-precision frequency response function and natural frequency, each measuring point was collected 10 times repeatedly, and the frequency response function was averaged in the frequency domain. The position of the test prototype is  $\theta(0) = [0, 90^\circ, 0, 0, 0, 0]^T$ , the bearing parameters is  $\mathbf{C}_b = \text{diag}(c_x, c_y, c_z, c_{\theta x}, c_{\theta y}, c_{\theta z})$  and  $\mathbf{K}_b = \text{diag}(k_x, k_y, k_z, k_{\theta x}, k_{\theta y}, k_{\theta z})$ . The remaining degrees of freedom of the bearing matrix are zero. Utilizing the subspace iteration method, the system's natural frequency and eigenvalue vector are determined, followed by the calculation of the modal effective mass. In the context of the series-parallel hybrid welding manipulator system, the combined effective mass of the initial three modes represents 82.86% of the total structure mass. Hence, validation of the first three modes is deemed satisfactory for this particular structure.

Table 1 summarizes the material characteristic parameters and moment of inertia of the welding manipulator. Table 2 summarizes the parameters of the first six motors and reducers of the system. Table 3 lists the bearing parameters. Table 4 compares the first three natural frequencies obtained from the proposed elastodynamic model and experimental tests. As can be seen from Table 4, the first-order natural frequency is very close, and the error is less than 1%. The errors of the last two natural frequencies do not exceed 5%. The results show that the established elastodynamic model is accurate and reliable; hence, it can serve as the basis for further vibration reduction analysis.

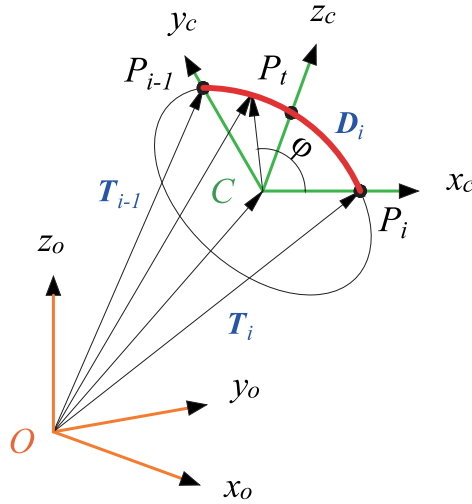


Fig. 8. The diagram of trajectory planning.

#### 4. Modeling and method of optimizing the planned trajectory

##### 4.1. Parameterization of arc paths in space

The schematic diagram of the position and attitude transformation from node  $i-1$  to node  $i$  is shown in Fig. 8, i.e.,  $T_{i-1}$  reaches  $T_i$  after the transformation, and the transformation relationship is given by

$$T_{i-1}D_i = T_i \quad (i = 1, 2, \dots, N) \quad (41)$$

$$D_i = \begin{bmatrix} \Delta R_i & \Delta p_i \\ \mathbf{0} & 1 \end{bmatrix} \quad (42)$$

where  $T_i$  denotes the transformation matrix,  $D_i$  denotes the position-attitude driving matrix,  $R_i$  denotes the attitude transformation matrix,  $\Delta R_i = R_{i-1}^T R_i$  denotes the attitude-driving matrix,  $p_i$  denotes the position transformation matrix, and  $\Delta p_i = R_{i-1}^T (p_i - p_{i-1})$  denotes the position-driving matrix.

Convert  $\Delta R_i$  to the form of the axis-angle parameter  $(k_i, \phi_i)$ , i.e.,

$$\Delta R_i = Rot(k_i, \phi_i) \quad (43)$$

$$\begin{cases} \phi_i = \arccos \frac{tr(\Delta R_i) - 1}{2} \\ k_i = \frac{1}{2\sin\phi_i} \begin{bmatrix} r_{i32} - r_{i23} \\ r_{i13} - r_{i31} \\ r_{i21} - r_{i12} \end{bmatrix} \end{cases} \quad (44)$$

where  $r_{ijk}$  denotes the  $(j, k)$ -th element in  $R_i$ ,  $k_i$  denotes the rotation axis in the  $\{x_{n(i-1)}, y_{n(i-1)}, z_{n(i-1)}\}$  system, and  $\phi_i$  denotes the equivalent rotation angle, which can be obtained according to the given  $R_{i-1}$  and  $R_i$ .

Let  $\Delta p_i = d_i$ . Then,  $D_i$  can be decomposed into the product of two homogeneous transformation matrices of translation and rotation:

$$D_i = \bar{L}(d_i) \bar{Rot}(k_i, \phi_i) \quad (45)$$

$$\begin{cases} \bar{L}(d_i) = \begin{bmatrix} I & d_i \\ \mathbf{0} & 1 \end{bmatrix} \\ \bar{Rot}(k_i, \phi_i) = \begin{bmatrix} Rot(k_i, \phi_i) & \mathbf{0} \\ \mathbf{0} & 1 \end{bmatrix} \end{cases} \quad (46)$$

It can be seen from Eq. (41) that the  $T_i$  between two nodes at any time can be obtained by the following driving changes:

$$T(t) = T_{i-1} \bar{L}(d_i) \bar{Rot}(k_i, \phi_i) \quad (t_{i-1} \leq t \leq t_i) \quad (47)$$

where  $t$  denotes any time between two points.

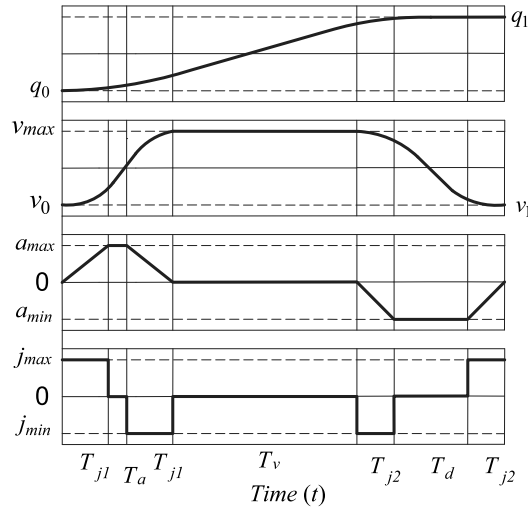


Fig. 9. Dual-S-curve motion profile.

**Table 5**  
Trajectory planning of interpolation function based on dual-S velocity profile.

$t$	$q(t)$	$\dot{q}(t)$	$\ddot{q}(t)$	$\ddot{q}(t)$
$t \in [0, T_{j1}]$	$q_0 + v_0 t + j_{max} \frac{t^3}{6}$	$v_0 + j_{max} \frac{t^2}{2}$	$j_{max} t$	$j_{max}$
$t \in [T_{j1}, T_d - T_{j1}]$	$q_0 + v_0 t + j_{max} \frac{a_{lim}}{6} (3t^2 - 3T_{j1}t + T_{j1}^2)$	$v_0 + j_{max} T_{j1} (t - \frac{T_{j1}}{2})$	$j_{max} T_{j1}$	0
$t \in [T_d - T_{j1}, T_d]$	$q_0 + (v_{lim} + v_0) \frac{T_d}{2} - v_{lim} (T_d - t)$	$v_{lim} + j_{max} \frac{(T_d - t)^2}{2}$	$-j_{min} (T_d - t)$	$j_{min}$
$t \in [T_d, T_d + T_{j1}]$	$q_0 + (v_{lim} + v_0) \frac{T_d}{2} + v_{lim} (t - T_d)$	$v_{lim}$	0	0
$t \in [T_d + T_{j1}, T_d + T_{j2}]$	$q_1 - (v_{lim} + v_1) \frac{T_d}{2} + v_{lim} (t - T_d)$	$v_{lim} - j_{max} \frac{(t - T_d)^2}{2}$	$-j_{max} (t - T_d)$	$j_{min}$
$t \in [T_d + T_{j2}, T_d + T_{j2} + T_{j2}]$	$q_1 - (v_{lim} + v_1) \frac{T_d}{2} + v_{lim} (t - T_d)$	$v_{lim} + a_{lim} (t - T_d - \frac{T_{j2}}{2})$	$-j_{max} T_{j2}$	0
$t \in [T_d + T_{j2} + T_{j2}, T]$	$q_1 - v_1 (T - t) - j_{max} \frac{(T - t)^3}{6}$	$v_1 + j_{max} \frac{(T - t)^2}{2}$	$-j_{max} (T - t)$	$j_{max}$

The boundary condition of the driving transformation matrix is expressed as follows:

$$D(t_{i-1}) = I, \quad D(t_i) = T_{i-1}^{-1} T_i \quad (48)$$

Therefore, the position-attitude interpolation problem between nodes is transformed into the interpolation problem of the equivalent rotation angle  $\phi(t)$  and the equivalent displacement  $d(t)$ . To ensure the coordination of the translational and rotational motions, a unified parameter is employed to describe the position and attitude.

The end of the robot moves from the initial posture to the terminal posture along the space arc, and the parametric equation is expressed as follows:

$$\begin{cases} d(\lambda) = R_{i-1}^T \lambda (p_i - p_{i-1}) & (0 \leq \lambda \leq 1) \\ \phi(\lambda) = \lambda \phi_i \end{cases} \quad (49)$$

where  $\lambda$  denotes path parameters.

Calculate the first-order and second-order derivatives of Eq. (49), and obtain the velocity and acceleration expressed in the base coordinate system. Therefore, by choosing an appropriate interpolation function  $\lambda(t)$ , an arc welding motion that satisfies both translational and rotational coordination can be obtained.

#### 4.2. Path parameter timing

According to the requirements of the actual continuous arc welding tasks of a welding robot, a dual-S velocity profile trajectory planning method is proposed. It is characterized by a step jerk curve in order to not only avoid sudden acceleration phenomena but also greatly reduce the stress and vibration effects on the transmission chain and load. The closed-loop synchronous control

scheme designed in Section 2.2 is utilized to control the displacement error and velocity error of the end trajectory. This scheme aims to minimize the synchronization error  $e = \xi_s - \xi_m$  and its derivative  $\dot{e} = \dot{\xi}_s - \dot{\xi}_m$  towards zero, thereby enhancing the accuracy of system motion control.

To minimize the total duration  $T$  of the planned trajectory, the maximum (minimum) values of the velocity, acceleration, and jerk should be reached as far as possible. Assuming that  $v_{\min} = -v_{\max}$ ,  $a_{\min} = -a_{\max}$ , and  $j_{\min} = -j_{\max}$ . Where  $j_{\max}$  and  $j_{\min}$  denote the maximum and minimum values of jerk respectively, and so on. Considering the case of  $q_t > q_s$ , define the maximum value of the actual achievable velocity during the movement as  $v_{\lim} = \max(\dot{q}(t))$ ,  $T_{j1}$  as the duration of constant jerk in the acceleration segment,  $T_{j2}$  as the duration of constant jerk in the deceleration segment,  $T_a$  as the acceleration cycle,  $T_v$  as the constant speed cycle,  $T_d$  as the deceleration cycle, and  $T$  as the total duration of the trajectory,  $T = T_a + T_v + T_d$ . When  $v_{\lim} = v_{\max}$ , judge whether the maximum acceleration is achievable according to the following conditions.

Assuming that  $(v_{\max} - v_0)j_{\max} \geq a_{\max}^2$ , the maximum acceleration value  $a_{\max}$  can be reached. The duration of the acceleration segment is expressed as follows:

$$T_{j1} = \sqrt{\frac{v_{\max} - v_0}{j_{\max}}}, \quad T_a = 2T_{j1} \quad (50)$$

Otherwise,

$$T_{j1} = \frac{a_{\max}}{j_{\max}}, \quad T_a = T_{j1} + \frac{v_{\max} - v_0}{a_{\max}} \quad (51)$$

Assuming that  $(v_{\max} - v_1)j_{\max} \geq a_{\max}^2$ , the minimum acceleration value  $a_{\min}$  can be reached. The duration of the deceleration segment is expressed as follows:

$$T_{j2} = \sqrt{\frac{v_{\max} - v_1}{j_{\max}}}, \quad T_d = 2T_{j2} \quad (52)$$

Otherwise,

$$T_{j2} = \frac{a_{\max}}{j_{\max}}, \quad T_d = T_{j2} + \frac{v_{\max} - v_1}{a_{\max}} \quad (53)$$

Finally, the duration of the constant velocity segment can be determined as follows:

$$T_v = \frac{q_1 - q_0}{v_{\max}} - \frac{T_a}{2} \left(1 + \frac{v_0}{v_{\max}}\right) - \frac{T_d}{2} \left(1 + \frac{v_1}{v_{\max}}\right) \quad (54)$$

If  $T_v > 0$ , the maximum velocity can actually be reached. The values obtained from Eq. (50) to Eq. (54) can be used for the trajectory calculation.

The interpolation function trajectory planning calculation method based on the dual-S velocity profile is shown in Fig. 9 and Table 5. According to the attitude transformation matrix  $T(t)$  at time  $t$ , the corresponding joint variable  $\theta$  can be solved using the inverse kinematics equation.

#### 4.3. Trajectory objective function

To suppress the elastic vibration at the end of the welding manipulator, improve the operation efficiency and reduce the energy consumption of the system as far as possible, a multi-objective trajectory optimization model is established considering the constraints of the joint angle, angular velocity, angular acceleration, and joint torque.

To improve the movement efficiency of the manipulator, the movement time objective function is established, which can be expressed as follows:

$$Ob_1 = T_a + T_v + T_d \quad (55)$$

where  $T_a$ ,  $T_v$  and  $T_d$  represent acceleration cycle, constant speed cycle and deceleration cycle, respectively.

As the core driving part of the welding robot arm, the joint accounts for the majority of the energy consumption. To minimize the energy consumption of the system, the corresponding energy consumption objective function is established as follows:

$$Ob_2 = \sum_{i=1}^n \int_{t_0}^{t_f} |\tau_i(t) \cdot \dot{\theta}_i(t)| dt \quad (56)$$

where  $n = 6$  denotes the number of joints of the manipulator;  $\dot{\theta}_i$  denote the velocity of the joint;  $\tau_i$  denote the moment of the joint.

To ensure the smooth operation of the welding task, the amplitude fluctuation of the terminal elastic vibration should not be too large. Therefore, the corresponding objective function of the terminal amplitude fluctuation is established as follows:

$$Ob_3 = \sum_{j=1}^n \sqrt{\frac{1}{t_f} \int_{t_0}^{t_f} (\epsilon_j(t) - \bar{\epsilon}_j)^2 dt} \quad (57)$$

where  $n = 6$  denotes the vibration linear displacement and vibration angular displacement of the end effector in the  $x$ ,  $y$ , and  $z$  directions, respectively;  $t_0$  and  $t_f$  denote the start and end times of the system rotation operation, respectively;  $\epsilon_j(t)$  and  $\bar{\epsilon}_j$  denote the elastic vibration displacement of the welding robot terminal and its average value, respectively.

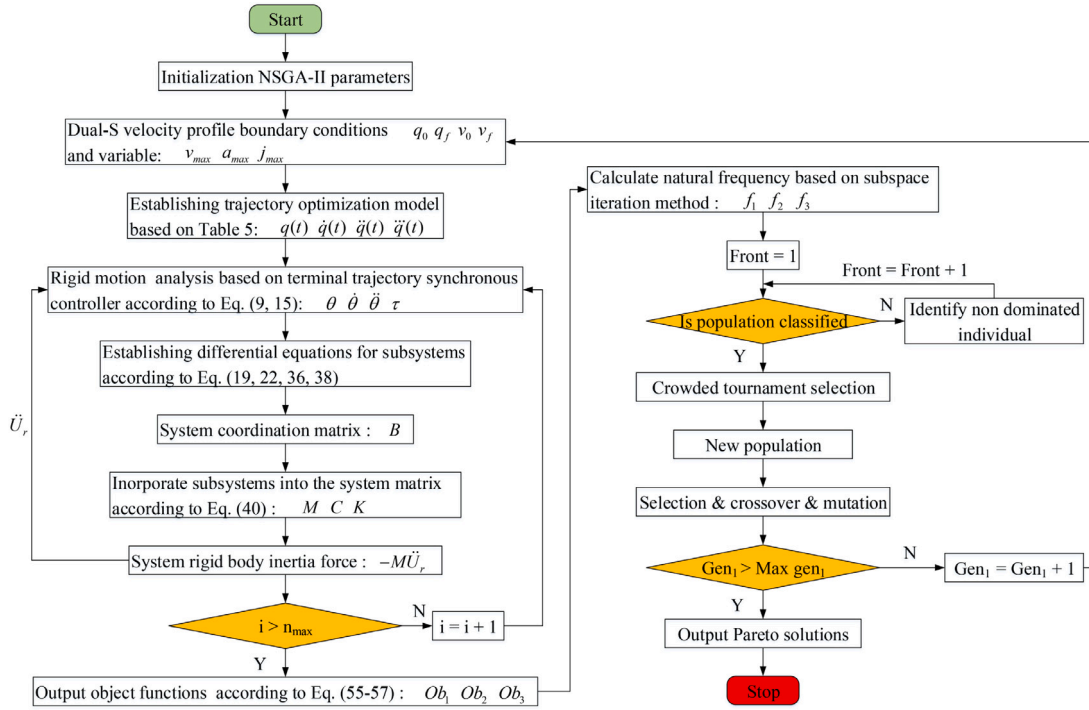


Fig. 10. Trajectory optimization flowchart of NSGA-II algorithm.

#### 4.4. Constraint condition

The kinematic constraints include limits on the joint angles, angular velocities, and angular accelerations, while the dynamic constraints are the actuator torques. To ensure the start-stop stability of the manipulator, the joint angular velocity and angular acceleration of the robot at the start-stop position are both zero. Establish the following constraints:

$$\begin{cases} |\theta_i| \leq \theta_{imax}, |\dot{\theta}_i| \leq \dot{\theta}_{imax}, |\ddot{\theta}_i| \leq \ddot{\theta}_{imax}, |\tau_i| \leq \tau_{imax} \\ \dot{\theta}_i(t_0, t_f) = 0, \ddot{\theta}_i(t_0, t_f) = 0 \end{cases} \quad (58)$$

where  $\theta_{max} = [160^\circ, 120^\circ, 70^\circ, 170^\circ, 90^\circ, 180^\circ]^T$ ,  $\dot{\theta}_{max} = 0.5$  rad/s, and  $\ddot{\theta}_{max} = 5$  rad/s<sup>2</sup> are the maximum values of the joint rotation angle, angular velocity, and angular acceleration, respectively, and  $\tau_{max} = [25, 12, 7.1, 16, 3, 5]^T$  Nm is the maximum value of the joint output torque.

Introducing the above constraints in the trajectory optimization prevents the joint movement of the welding robot from exceeding the limit when performing tasks and avoids high joint torque that might cause damage to the motor, thereby ensuring the safety and reliability of the welding robot.

#### 4.5. Optimal algorithm of vibration suppression based on NSGA-II

The second-generation non-dominated sorting optimization algorithm (NSGA-II) is proposed based on the NSGA algorithm, which overcomes the problems of the NSGA algorithm's lack of elite selection mechanism, need to select the best shared parameter values, and low optimization efficiency. In general, the NSGA-II algorithm adopts the elite strategy when selecting the next-generation population and performs non-dominated stratification according to the dominance relationship between chromosome individuals, which enables the elite individuals to have a greater chance of being inherited by the next generation. In addition, the fitness sharing strategy can ensure even distribution of the individuals when looking for the Pareto front, which is conducive to maintaining the diversity of the population, overcoming the over-breeding of super individuals, and preventing the premature phenomenon.

In this section, the NSGA-II algorithm based on the genetic algorithm is used to optimize the arc trajectory of the hybrid welding manipulator in the Cartesian space with the goal of optimizing the time, energy consumption, and terminal amplitude fluctuation. Thus, the Pareto optimal solution set of the system is obtained. The algorithm for welding trajectory optimization of the manipulator is described in Fig. 10.

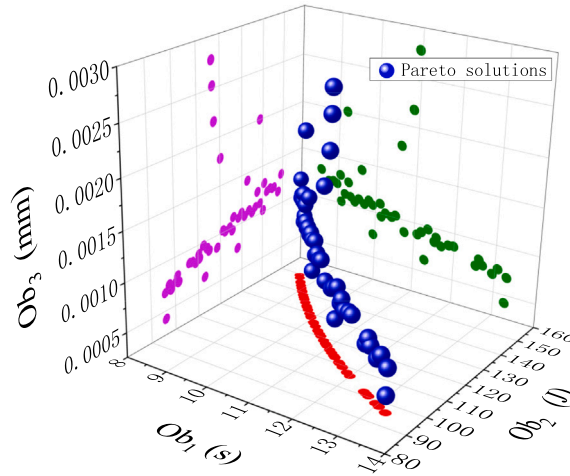


Fig. 11. Distribution of Pareto optimal front.

**Table 6**  
Solutions of Pareto optimal front.

Scheme	$v_{max}$ (rad s <sup>-1</sup> )	$a_{max}$ (rad s <sup>-2</sup> )	$j_{max}$ (rad s <sup>-3</sup> )	$Ob_1$ (s)	$Ob_2$ (J)	$Ob_3$ (mm)
A	0.044	0.037	0.045	<b>8.629</b>	147	0.001143
B	0.035	0.036	0.016	11.281	113	<b>0.000631</b>
C	0.029	0.016	0.014	13.065	<b>98</b>	0.000754

## 5. Numerical simulation

To illustrate the effectiveness and feasibility of the trajectory planning method proposed to indirectly suppress vibration. The goals include achieving the shortest time, lowest energy consumption, and smallest amplitude. The variables considered are maximum velocity, maximum acceleration, and maximum jerk of the trajectory, while constraints involve joint angles, angular velocity, angular acceleration, and joint torque. The NSGA-II is implemented in MATLAB to solve the model of multi-objective trajectory optimization.

### 5.1. Parameter settings

During the continuous arc welding process, the radius of the circle is  $R = 0.6$  m, and the coordinates of the center of the circle are  $P_c = [0.300, 0.495, 0.554]^T$ . The manipulator moves from the initial pose and then stops at the final pose are respectively as follows:  $P_0 = [0, 60^\circ, 0, 0, -60^\circ, 0]^T$ ,  $P_f = [5^\circ, 45^\circ, 12^\circ, 15^\circ, -67^\circ, 0]^T$ . The welding velocity of a six-degree-of-freedom welding manipulator is generally 50 to 160 cm/min. Therefore, the value range of the maximum velocity (m/s), maximum acceleration (m/s<sup>2</sup>) and maximum jerk (m/s<sup>3</sup>) of the trajectory is set to  $[0.0281, 0.0157, 0.0136]^T \leq [v_{max}, a_{max}, j_{max}]^T \leq [0.0445, 0.0376, 0.0454]^T$ . The initialization parameters of NSGA-II are as follows: population size = 50, number of iterations = 50. For constrained optimization problems, the distribution exponents of the real coded crossover and mutation operators are both 20.

### 5.2. Results and discussion

The optimal Pareto frontier solution set distribution is shown in Fig. 11. Three representative groups of solutions with the smallest driving time (scheme A), the lowest energy consumption (scheme C), and the smallest amplitude fluctuation (scheme B) were selected. The corresponding values of the three variables and the three objective functions are listed in Table 6. Among the Pareto solutions, scheme A requires the shortest time, i.e., 8.629 s. Using this solution, the hybrid welding manipulator can complete the welding task in a shorter time with higher operating efficiency. However, owing to the continuous output power of the motor, it consumes more energy, i.e., 147 J, which causes increased oscillation of the end effector, and the terminal amplitude fluctuation is 0.001143 mm. Scheme C has the longest working time, i.e., 13.065 s. However, the motor output power is stable and the energy consumption is minimal. The energy consumption is only 98 J, and the corresponding terminal amplitude fluctuation is 0.000754 mm. Obviously, the two objectives of the shortest movement time and the minimum energy consumption are in conflict with each other. In other words, excessively focusing on efficiency will lead to excessive mechanical energy consumption. The duration of exercise in scheme B is shorter than that in scheme C; however, the energy consumption is less than that of scheme A, the fluctuations are smaller, the joint torque changes smoothly, and the quality of the mechanism welding operation is the highest. In



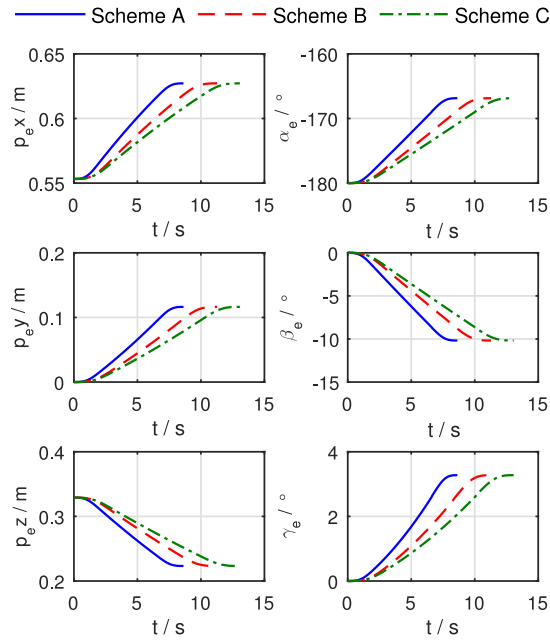


Fig. 12. Position and attitude angle of the end effector.

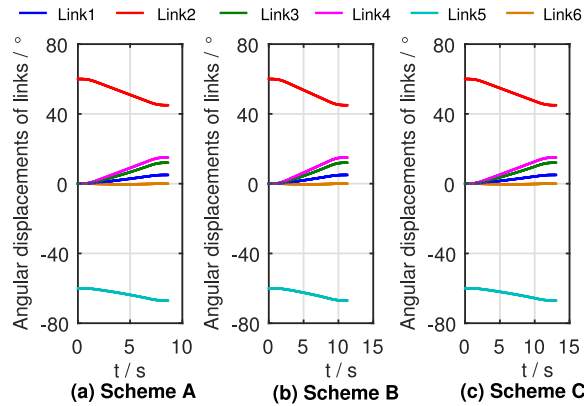


Fig. 13. Angular displacement of the links.

summary, scheme *B* can relatively optimize the three indicators of time, energy consumption, and terminal oscillation. Its duration is 11.281 s, energy consumption is 113 J, and terminal amplitude fluctuation is 0.000631 mm.

For the three different solutions, the position trajectories of the welding manipulator end effector in the  $x$ ,  $y$ , and  $z$  directions and the azimuth trajectories of the Euler angles  $\alpha$ ,  $\beta$ , and  $\gamma$  are calculated and obtained, as shown in Fig. 12. In the initial posture and target posture, all the movement paths are relatively continuous and smooth, meeting the posture requirements of the starting and ending points of movement.

According to the motion trajectory of Cartesian space planning, the motion trajectory of each actuator can be obtained using the inverse kinematics model. Under the three schemes, the angular displacement, angular velocity, angular acceleration, and torque curves of the link joints are shown in Figs. 13–16. In the initial attitude and the target attitude, the values of the velocity and acceleration components are zero, and the joint torque meets the requirements of the actuator and is within the constraint range, which is consistent with the set arc welding task.

By integrating the elastodynamic equations, the elastic linear displacements and the elastic angular displacements in the three directions are obtained, as shown in Fig. 17. The elastic vibration in the  $x$  and  $z$  directions is larger than that in the  $y$  direction, which proves that the mechanism moves in the  $xoz$  plane.

To further verify the effectiveness of the proposed method, a comparative study was conducted by considering the space arc trajectory of the hybrid welding manipulator planned via fifth-order polynomial (FP) planning as an example. To compare the results

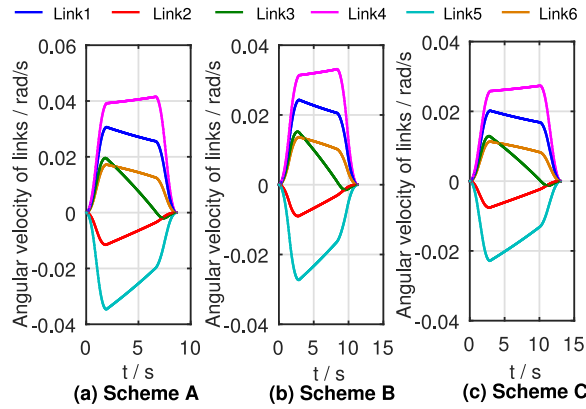


Fig. 14. Angular velocity of the links.

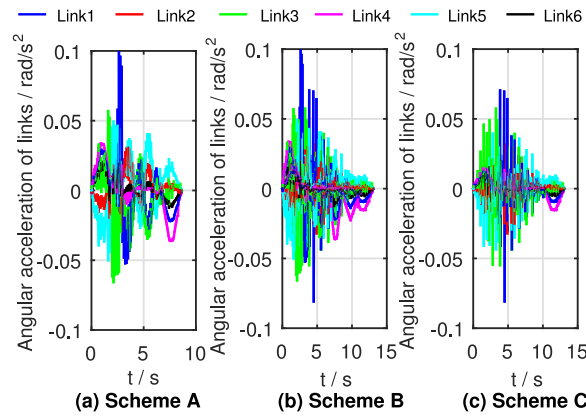


Fig. 15. Angular acceleration of the links.

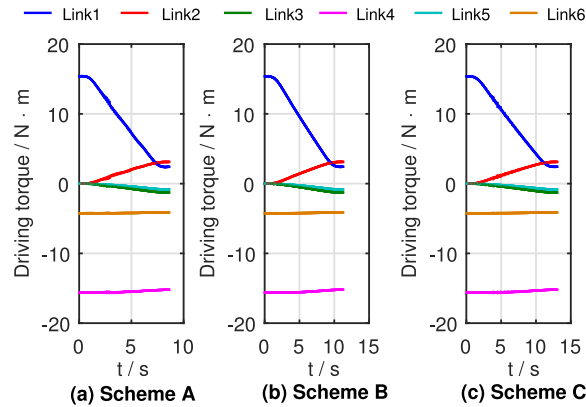


Fig. 16. Driving torque of each joint.

obtained by the two methods, the total travel time was set to be consistent with the proposed scheme *B*. In addition, the velocity and acceleration at the start and end points were set to zero.

Fig. 18 shows the comparison curve of the objective function obtained using the fifth-degree polynomial trajectory function and the proposed scheme *B*. The total energy consumption of the FP scheme is 113.06 J, and the total energy consumption of scheme *B* is 113 J, which represents a 0.05% reduction in energy consumption. The average fluctuation of the terminal amplitude of the FP scheme is 0.001109 mm, and the average fluctuation of the terminal amplitude of scheme *B* is 0.000631 mm, which represents a

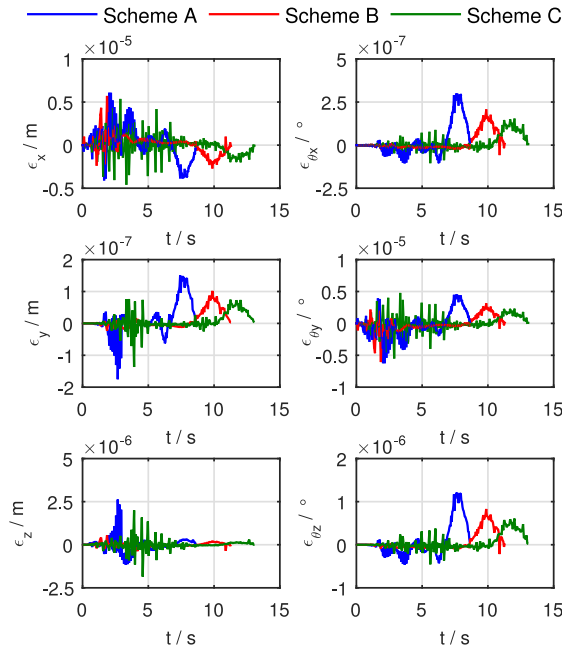


Fig. 17. Elastic displacement of the end effector.

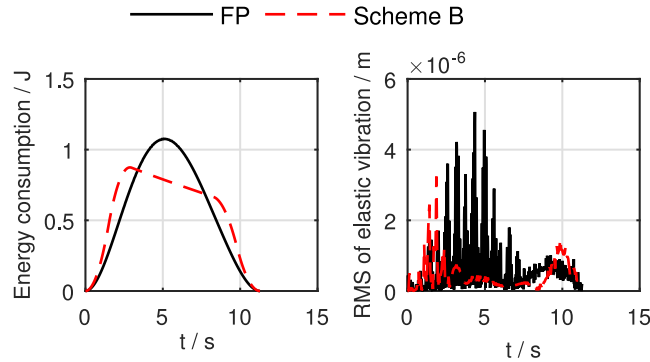


Fig. 18. Comparison chart of objective function. (a) Energy consumption; (b) Elastic vibration variance.

43% reduction. The simulation results confirm that the proposed multi-objective optimization method effectively reduces the system terminal vibration amplitude and has broad applicability.

## 6. Conclusion

In this paper, a multi-objective approach that effectively suppress the vibration for the complex series-parallel hybrid flexible welding manipulator is proposed to gain faster time, lower energy consumption and higher stability performance in continuous arc welding motion task. The main conclusions are the following: (I) A comprehensive elastodynamics equation of the system involved in multi-kinematic pair arrangements and multi-motor drives was established, and the effectiveness of the model was verified using the hammer test method. (II) Based on the dual-S velocity interpolation function and the synchronous planning controller, the coordination of the end position and attitude was achieved. (III) To achieve a trade-off among the three objective functions, the optimized solution under simulation conditions was obtained, *i.e.*, the total movement time was 11.28 s, the system energy consumption was 113 J, and the terminal amplitude fluctuation was 0.000631 mm. Compared with the classical fifth-degree polynomial trajectory planning, the energy consumption was basically the same while the amplitude fluctuation was reduced by 43%.

The proposed method can also be applied to other types of robotic equipment. However, for the mechanical dynamics system of the manipulator, the mathematical model has unknown model errors and interferences, such as various high-frequency vibration characteristics, joint friction, signal detection errors and other uncertain factors, which are all causes of model errors. In the future, we will improve the accuracy of modeling and design corresponding controllers.

## CRediT authorship contribution statement

**Caixia Ban:** Writing – review & editing, Writing – original draft, Validation, Software, Methodology, Formal analysis, Conceptualization. **Bing Fu:** Validation, Software. **Wei Wei:** Writing – review & editing. **Zhaotao Chen:** Resources, Methodology, Conceptualization. **Shengnan Guo:** Methodology, Conceptualization. **Nianchun Deng:** Project administration, Methodology, Conceptualization. **Lili Yuan:** Methodology, Conceptualization. **Yu Long:** Writing – review & editing, Supervision, Resources, Project administration, Methodology, Funding acquisition, Conceptualization.

## Declaration of competing interest

The authors declare that they have no known competing financial interests or personal relationships that could have appeared to influence the work reported in this paper.

## Data availability

No data was used for the research described in the article.

## Acknowledgments

We would like to express our sincere thanks to the editor and anonymous reviewers for their useful comments and suggestions, which helped to substantially improve the manuscript. This work was supported by the Key R and D Program of Guangxi Province (Grant No. GKAB23026101), Transportation Operation Subsidy Project of Guangxi Key Laboratory of International Join for China-ASEAN Comprehensive Transportation in 2021 (No. 21-220-21), Guangxi Natural Science Foundation (Grant No. 2023GXNSFBA026287), Guangxi Natural Science Foundation (2020JJB160014), and Guangxi Postdoctoral Innovative Talent Support Program.

## References

- [1] S. Erkaya, Investigation of joint clearance effects on welding robot manipulators, *Robot. Comput.-Integr. Manuf.* 28 (4) (2012) 449–457.
- [2] J. Qin, F. Leonard, G. Abba, Real-time trajectory compensation in robotic friction stir welding using state estimators, *IEEE Trans. Control Syst. Technol.* 24 (6) (2016) 2207–2214.
- [3] Z. Hu, L. Hua, X. Qin, M. Ni, Z. Liu, C. Liang, Region-based path planning method with all horizontal welding position for robotic curved layer wire and arc additive manufacturing, *Robot. Comput.-Integr. Manuf.* 74 (2022) 102286.
- [4] A. Rout, B.B.V.L. Deepak, B.B. Biswal, G.B. Mahanta, Weld seam detection, finding, and setting of process parameters for varying weld gap by the utilization of laser and vision sensor in robotic arc welding, *IEEE Trans. Ind. Electron.* 69 (1) (2022) 622–632.
- [5] S. Yue, Redundant robot manipulators with joint and link flexibility .1. Dynamic motion planning for minimum end effector deformation, *Mech. Mach. Theory* 33 (1–2) (1998) 103–113.
- [6] S. Yue, Redundant robot manipulators with joint and link flexibility .2. Residual vibration decreasing, *Mech. Mach. Theory* 33 (1–2) (1998) 115–122.
- [7] S.K. Dwivedy, P. Eberhard, Dynamic analysis of flexible manipulators, a literature review, *Mech. Mach. Theory* 41 (7) (2006) 749–777.
- [8] C.T. Kiang, A. Spowage, C.K. Yoong, Review of control and sensor system of flexible manipulator, *J. Intell. Robot. Syst.* 77 (1, SI) (2015) 187–213.
- [9] L. Malgaca, H. Dogan, M. Akdag, S. Yavuz, M. Uyar, B. Bidikli, Effect of joint flexibility on vibration characteristics of a composite box manipulator, *Compos. Struct.* 183 (SI) (2018) 271–277.
- [10] L. Malgaca, M. Uyar, Hybrid vibration control of a flexible composite box cross-sectional manipulator with piezoelectric actuators, *Compos. Pt. B-Eng.* 176 (2019) 107278.
- [11] Q. Su, W. Chen, J. Deng, X. Tian, Y. Liu, A 3-DOF sandwich piezoelectric manipulator with low hysteresis effect: Design, modeling and experimental evaluation, *Mech. Syst. Signal Proc.* 158 (2021) 107768.
- [12] N. Mishra, S.P. Singh, Determination of modes of vibration for accurate modelling of the flexibility effects on dynamics of a two link flexible manipulator, *Int. J. Non-Linear Mech.* 141 (2022) 103943.
- [13] Y. Zhao, J. Mei, W. Niu, Vibration error-based trajectory planning of a 5-dof hybrid machine tool, *Robot. Comput.-Integr. Manuf.* 69 (2021) 102095.
- [14] Y. Xu, Z. Teng, J. Yao, Y. Zhou, Y. Zhao, Elastodynamic analysis of a novel motion-decoupling forging manipulator, *Mech. Mach. Theory* 147 (2020) 103771.
- [15] C. Ban, G. Cai, W. Wei, S. Peng, Dynamic response and chaotic behavior of a controllable flexible robot, *Nonlinear Dyn.* 109 (2) (2022) 547–562.
- [16] J. Gong, G. Cai, W. Wei, K. Zhang, S. Peng, Research on the residual vibration suppression of a controllable mechanism robot, *IEEE Access* 10 (2022) 39436–39455.
- [17] M. Wu, J. Mei, Y. Zhao, W. Niu, Vibration reduction of delta robot based on trajectory planning, *Mech. Mach. Theory* 153 (2020) 104004.
- [18] X. Wang, J.K. Mills, Dynamic modeling of a flexible-link planar parallel platform using a substructuring approach, *Mech. Mach. Theory* 41 (6) (2006) 671–687.
- [19] H. Gao, W. He, C. Zhou, C. Sun, Neural network control of a two-link flexible robotic manipulator using assumed mode method, *IEEE Trans. Ind. Inform.* 15 (2) (2019) 755–765.
- [20] J. Chou, I. Horng, W. Liao, Robust observer-based OMF vibration control of flexible linkage mechanisms using piezoelectric films, *Int. J. Mech. Sci.* 40 (8) (1998) 749–759.
- [21] Z. Mohamed, M. Tokhi, Command shaping techniques for vibration control of a flexible robot manipulator, *Mechatronics* 14 (1) (2004) 69–90.
- [22] R. Theodore, A. Ghosal, Robust control of multilink flexible manipulators, *Mech. Mach. Theory* 38 (4) (2003) 367–377.
- [23] Z. Wang, Y. Li, P. Sun, Y. Luo, B. Chen, W. Zhu, A multi-objective approach for the trajectory planning of a 7-DOF serial-parallel hybrid humanoid arm, *Mech. Mach. Theory* 165 (2021) 104423.
- [24] S. Yavuz, L. Malgaca, H. Karagulle, Vibration control of a single-link flexible composite manipulator, *Compos. Struct.* 140 (2016) 684–691.
- [25] H. Karagulle, L. Malgaca, M. Dirilmis, M. Akdag, S. Yavuz, Vibration control of a two-link flexible manipulator, *J. Vib. Control* 23 (12) (2017) 2023–2034.
- [26] C. Dong, L. Shiqi, W. JunFeng, F. Yi, L. Yang, A multi-objective trajectory planning method based on the improved immune clonal selection algorithm, *Robot. Comput.-Integr. Manuf.* 59 (2019) 431–442.

- [27] A. Abe, Trajectory planning for residual vibration suppression of a two-link rigid-flexible manipulator considering large deformation, *Mech. Mach. Theory* 44 (9) (2009) 1627–1639.
- [28] T. Chen, J. Lou, Z. Ren, Y. Wei, Optimal switching time control for suppressing residual vibration in a high-speed macro-micro manipulator system, *IEEE Trans. Control Syst. Technol.* 30 (1) (2022) 360–367.
- [29] E. Spyrakos-Papastavridis, J.S. Dai, Minimally model-based trajectory tracking and variable impedance control of flexible-joint robots, *IEEE Trans. Ind. Electron.* 68 (7) (2021) 6031–6041.
- [30] D. Lee, C.-W. Ha, Optimization process for polynomial motion profiles to achieve fast movement with low vibration, *IEEE Trans. Control Syst. Technol.* 28 (5) (2020) 1892–1901.
- [31] X. Li, X. Gao, J. Xiao, H. Cheng, Y. Zhang, L. Hao, Time-optimal general asymmetric S-curve profile with low residual vibration, *Mech. Syst. Signal Proc.* 188 (2023) 109978.
- [32] A. Alzaydi, Time-optimal, minimum-jerk, and acceleration continuous looping and stitching trajectory generation for 5-axis on-the-fly laser drilling, *Mech. Syst. Signal Proc.* 121 (2019) 532–550.